The role of charge recombination to triplet excitons in organic solar cells

Alexander J. Gillett[1], Alberto Privitera[2], Rishat Dilmurat[3], Akchheta Karki[4], Deping Qian[5], Anton Pershin[3,6], Giacomo Londi[3], William K. Myers[7], Jaewon Lee[4,8], Jun Yuan[5,9], Seo-Jin Ko[4,10], Moritz K. Riede[2], Feng Gao[5], Guillermo C. Bazan[4], Akshay Rao[1], Thuc-Quyen Nguyen[4*], David Beljonne[3*] and Richard H. Friend[1*].*

[1]Cavendish Laboratory, University of Cambridge, JJ Thomson Avenue, Cambridge, CB3 0HE, UK.

[2]Clarendon Laboratory, University of Oxford, Parks Road, Oxford, OX1 3PU, UK.

[3]Laboratory for Chemistry of Novel Materials, Université de Mons, Place du Parc 20, 7000 Mons, Belgium.

[4]Centre for Polymers and Organic Solids, Department of Chemistry and Biochemistry, University of California at Santa Barbara, CA 93106, USA.

[5]Department of Physics, Chemistry and Biology (IFM), Linköping University, Linköping, 58183, Sweden.

[6]Wigner Research Centre for Physics, PO Box 49, H-1525, Budapest, Hungary.

[7]Centre for Advanced ESR, Inorganic Chemistry Laboratory, University of Oxford, South Parks Road, Oxford, OX1 3QR, UK.

[8]Department of Chemical Engineering and Applied Chemistry, Chungnam National University, 99, Daehak-ro, Yuseong-gu, Daejeon, 34134, Republic of Korea.

[9]College of Chemistry and Chemical Engineering, Central South University, Changsha, 410083, P.R. China.

[10]Division of Advanced Materials, Korea Research Institute of Chemical Technology, Daejeon 34114, Republic of Korea.

[*]Corresponding authors: Alexander J. Gillett: E-mail: ajg216@cam.ac.uk; Thuc-Quyen Nguyen: E-mail: quyen@chem.ucsb.edu; David Beljonne: E-mail: david.beljonne@umons.ac.be; Richard H. Friend: E-mail: rhf10@cam.ac.uk.

The power conversion efficiencies (PCEs) of organic solar cells (OSCs) using non-fullerene acceptors (NFAs) have now reached 18%[1]. However, this is still lower than inorganic solar cells, for which PCEs >20% are commonplace[2]. A key reason is that OSCs still show low open-circuit voltages (V_{OC}) relative to their optical band gaps[3], attributed to non-radiative recombination[4]. For OSCs to compete with inorganics in efficiency, all non-radiative loss pathways must be identified and where possible, removed. Here, we show that in most NFA OSCs, the majority of charge recombination at open-circuit proceeds *via* formation of non-emissive NFA triplet excitons (T_1); in the benchmark PM6:Y6 blend[5], this fraction reaches 90%, contributing 60 mV to the reduction of V_{OC}. We develop a new design to prevent recombination *via* this non-radiative channel through the engineering of significant hybridisation between the NFA T_1 and the spin-triplet charge transfer exciton (^{3}CTE). We model that the rate of the back charge transfer from ^{3}CTE to T_1 can be reduced by an order of magnitude, allowing re-dissociation of the ^{3}CTE. We then demonstrate NFA systems where T_1 formation is suppressed. This work therefore provides a clear design pathway for improved OSC performance to 20% PCE and beyond.

Within the Shockley-Queisser model, an ideal solar cell should possess only radiative recombination, thus also acting as an ideal light emitting diode with 100% electroluminescence external quantum efficiency (EQE_{EL})[4,6–8]. This sets the limit to the photon energy loss (ΔE_{loss}), defined as the difference between the optical band gap (E_g) and the energy of the extracted charges (qV_{OC})[4]. However, when the EQE_{EL} falls below 1, non-radiative recombination incurs an additional voltage loss (ΔV_{nr})[7,8]:

$$\Delta V_{nr} = \frac{-k_B T}{q} ln(EQE_{EL}) \quad (1)$$

where k_B is the Boltzmann constant, T is temperature and q is the elementary charge. In most non-fullerene acceptor (NFA) organic solar cells (OSCs), EQE_{EL} is currently ~10^{-4}-10^{-5}, giving ΔV_{nr} ~230-290 mV and ΔE_{loss} =500-600 meV[3,9–12]. Thus, for PCEs >20% to be achieved in OSCs, ΔE_{loss} must be reduced[13,14], with ΔV_{nr} the key area for improvement[13,15]. To better understand the factors controlling the EQE_{EL}, it is useful to separate the different contributions[16]:

$$EQE_{EL} = \gamma \Phi_{PL} \chi \eta_{out} \tag{2}$$

where γ is the charge balance factor (often engineered to be ~1), Φ_{PL} is the photoluminescence quantum efficiency, χ is the fraction of recombination events that can decay radiatively (excitons in the spin-singlet configuration, S_1) and η_{out} is the photon out-coupling efficiency (typically ~0.3). Here, the two key factors that can be manipulated are Φ_{PL} and χ. For OSCs, we treat Φ_{PL} as equivalent to the luminescence yield of spin-singlet excitations. In an efficient OSC, almost all photo-generated S_1 dissociate into free charges (FCs); photon emission will occur following FC recombination. Thus, in the situation where recombination is able to proceed *via* the S_1 state of the lowest E_g component[11,17], we consider that Φ_{PL} of the neat low E_g material will set the upper limit for Φ_{PL} in an OSC blend. Whilst the recent empirical advances in EQE_{EL} have been achieved by raising Φ_{PL}[11,13,18,19], here, we address the role of χ in NFA OSCs.

In OSCs, the recombination of FCs proceeds *via* the formation of charge transfer excitons (CTEs), with an electron on the acceptor (A) and a hole on the donor (D) material. These CTEs will be created in a 1:3 ratio of spin-singlet (^{1}CTE) and spin-triplet (^{3}CTE) states *via* spin-statistical non-geminate recombination[20]. However, OSC systems studied to date possess molecular triplet states (T_1) lower in energy than the ^{3}CTE on either the D or A. Thus, it is possible for back charge transfer (BCT) from ^{3}CTE to T_1 to occur[21–23]. Since the S_1-T_1 energy gap in most organic semiconductors is ~0.6–1 eV[24], T_1 will be too low in energy to thermally re-dissociate and must decay non-radiatively[25], resulting in χ <1 and an increased ΔV_{nr}[26]. To understand whether a system will generate T_1, it is necessary to analyse the competing processes that can occur from the ^{3}CTE. This includes BCT, re-dissociation into FCs, and conversion to ^{1}CTE. We note that ^{3}CTE-^{1}CTE conversion, with a typical rate of 10^8-10^6 s^{-1}, is too slow to compete with the other pathways (*vide infra*)[27]. Thus, T_1 formation from ^{3}CTE is determined by the competition between the rates of BCT (k_{BCT}) and re-dissociation ($k_{dissociation}$) of ^{3}CTE[22,28]. Furthermore, as ^{3}CTEs can be formed from both geminate[29,30] (Fig. 1a) and non-geminate[22,31,32] (Fig. 1b) charge carrier pairs, it is also important to consider that BCT to T_1 can occur through two distinct mechanisms.

In OSCs that use fullerenes as electron acceptors, T_1 generation is generally observed and has already been extensively studied, though the impact on device performance is debated[22,26,29–31,33–35]. In this work, we address the role of triplet states in NFA OSCs by examining nine high performance systems. The structures of the four polymer donors and seven NFAs used in this study are shown in Fig. 1c. A summary of device performance (current density-voltage and EQE_{EL} curves in Figs. S2-S3), Φ_{PL} for a neat film of the relevant NFA, ΔV_{nr}, and whether the blend exhibits geminate or non-geminate T_1 formation are given in Table 1. We find that geminate T_1 formation, as determined by transient electron paramagnetic resonance (trEPR) spectroscopy, is not observed in our NFA blends. However, non-geminate T_1 formation, probed through transient absorption (TA) spectroscopy, is generally seen, with the exception of the closely-related PTB7-Th:IEICO-0F and PTB7-Th:IEICO-2F systems.

Two NFA blends were selected to act as representative case studies; PM6:Y6 as one of the best performing OSC systems[5], despite exhibiting non-geminate T_1 formation, and PTB7-Th:IEICO-2F, which has no detectable BCT T_1. A full account of all other blends is in the SI.

Fig. 2a shows the TA of PM6:Y6, pumped at 532 nm for preferential PM6 excitation. Here, we focus solely on the infrared probe spectral region where the photo-induced absorptions (PIAs) of T_1 states are typically found (full spectral range TA in Fig. S14)[22]. At 0.1-0.2 ps after excitation, we observe PIA bands at 1250 nm and 1550 nm; though comparison to the TA of the neat materials (Figs. S5-6), these are respectively assigned to the PM6 S_1 and an intermolecular excitation between neighbouring Y6 molecules[36]. As charge transfer develops, these features are lost and a new PIA at 1450 nm grows beyond a few picoseconds, confirmed to be the Y6 T_1 by triplet sensitisation experiments (Fig. S4b). Kinetics from the T_1 spectral region (Fig. 2b) show a strong fluence dependence in T_1 formation, demonstrating that triplets are generated *via* bimolecular processes. Deviation of the T_1 region kinetics of the lowest and highest fluences begins on sub-picosecond timescales, demonstrating that non-geminate recombination can occur extremely quickly when the excitation fluence is high; from this, we can infer that k_{BCT} of the interfacial ^{3}CTE must be $\sim10^{11}$-10^{12} s^{-1}. To determine $k_{dissociation}$, we have fitted the growth of the electro-absorption feature of the donor polymer in multiple blends (Figs. S29-S34), which is signature for the separation of interfacial CTEs into FCs[37–39]. Fitting reveals that $k_{dissociation}$ of the thermalized interfacial CTEs is between 10^{10}-10^{11} s^{-1} for the NFA blends studied here. Thus, we can rationalise why T_1 is observed in PM6:Y6 as $k_{BCT} >> k_{dissociation}$. Furthermore, utilising a previously employed kinetic model (full details in SI), we determine that ~90% of the recombination in this blend under conditions equivalent to open-circuit (no carriers are extracted from the film) proceeds non-radiatively *via* the Y6 T_1 (Fig. S37). The T_1 recombination fraction can be greater than the 75% predicted by spin-statistics as CTEs form and separate multiple times prior to recombining[31,40]. We note that the presence of non-geminate T_1 formation in PM6:Y6 is representative of most NFA blends studied in this work.

When recombination via T_1 is present, it will accelerate the recombination of FCs *via* CTEs by providing an additional deactivation pathway. However, it has been reported that the bimolecular recombination rates of efficient NFA OSCs are significantly reduced from the Langevin rate[41,42]. In our TA measurements, we only detect the terminal recombination mechanism, not the preceding unsuccessful recombination attempts. Therefore, the high k_{BCT} we measure is only relevant for ^{3}CTEs at the D:A interface where rapid BCT to T_1 is favoured. Consistent with the large Langevin reduction factors reported, most recombination attempts must therefore be taking place at increased electron-hole separations where $k_{dissociation} >> k_{BCT}$, enabling rapid thermal ^{3}CTE re-dissociation. However, under open-circuit conditions, thermodynamics is the sole factor determining ΔV_{nr}[7,8]. Thus, the only relevant consideration for ΔV_{nr} is the final state through which terminal recombination takes place, not the kinetics of the preceding processes.

We next turn to trEPR to investigate geminate T_1 pathways. Fig. 2c shows the trEPR spectra of PM6:Y6 after 532 nm excitation (full discussion in Fig. S53). At 1 μs, we observe a single, intense peak at 346 mT that can be attributed to FCs[43] and a broader weak triplet feature. However, at 5 μs there are no remaining triplet signals, likely due to the rapid triplet-charge annihilation in this blend (Fig. S38). The triplet detected at 1 μs can be simulated by a single *eeeaaa* (*e* =emission, *a* =absorption) species, characteristic of T_1 formed *via* intersystem crossing (ISC) mediated by spin-orbit coupling (SOC)[23,44,45]; we attribute this T_1 to ISC from un-dissociated S_1 states. Importantly, the absence of any triplet species with an *aeeaae* or *eaaeea* polarisation pattern, a clear and unique fingerprint of the geminate BCT pathway[23,44,45], confirms that geminate T_1 formation does not occur in this blend. This is a characteristic observation of all the NFA OSC systems studied.

We now focus on PTB7-Th:IEICO-2F, an NFA blend where T_1 generation from CTEs could not be detected; its TA is shown in Fig. 2d (excitation at 620 nm preferentially pumped PTB7-Th). In the infrared probe region (full spectral range data in Fig. S17), two distinct PIA features at 1175 nm and 1550 nm are observed at the earliest time of 0.2-0.3 ps. Through comparison to the TA of the neat materials (Figs. S7-S8), we assign the feature at 1175 nm to the edge of the IEICO-2F S_1 and the 1550 nm band to the PTB7-Th S_1. As charge transfer develops, both PIAs are lost and only the edge of the PTB7-Th hole PIA is visible at 1175 nm. Importantly, there is no detectable formation of the IEICO-2F T_1 PIA, found to be at 1350 nm from triplet sensitisation measurements (Fig. S4c). Furthermore, there is no fluence dependence of the kinetics taken from the IEICO-2F T_1 region (Fig. 2e), providing additional evidence that non-geminate T_1 formation is not a detectable recombination pathway.

In the trEPR of PTB7-Th:IEICO-2F excited at 532 nm (Fig. 2f, full discussion in Fig. S57), we observe a prominent SOC-ISC T_1 feature with a clear *eeeaaa* polarisation pattern that inverts to *aaaeee* by 5 μs[23,44,45], as well as an *ea* polarisation ^{3}CTE at 346 mT that evolves into FC[23]. The T_1 spectral inversion by 5 μs is due to differing decay rates from the three high-field triplet levels[46]. To explain the increased ISC T_1 intensity in PTB7-Th:IEICO-2F, we note that the IEICO derivatives exhibit relatively high ISC quantum yields of ~5% (Fig. S35), meaning substantial T_1 formation from any un-dissociated S_1 is expected. However, geminate BCT T_1 states are absent.

We next evaluate the impact of T_1 formation on device performance. In PM6:Y6, we have shown that ~90% of the recombination at open-circuit proceeds non-radiatively *via* the Y6 T_1; this equates to χ =0.1, reducing the EQE_{EL} by a factor of ten. From equation 1, this increases ΔV_{nr} by ~60 mV. We corroborate this ΔV_{nr} increase in the PTB7-Th:IEICO-2F and PTB7-Th:IEICO-4F blends, where only PTB7-Th:IEICO-4F exhibits non-geminate T_1 formation (Fig. S26), due to a poorer energy alignment between ^{3}CTE and T_1 (Fig. S66). Here, the NFA structures differ only by two fluorine atoms and the NFA S_1 (PTB7-Th blend ^{1}CTE) energies are 1.36 and 1.34 eV (1.29 and 1.26 eV) for IEICO-2F and IEICO-4F, respectively (Fig. S62). This enables a direct appraisal of the contribution from T_1 formation to ΔV_{nr} without a significant influence of molecular structure, Φ_{PL}, the absolute energies of S_1 and ^{1}CTE, and the S_1-^{1}CTE offset[17,47]. A ΔV_{nr} =0.28 V is obtained for PTB7-Th:IEICO-2F, whereas ΔV_{nr} =0.34 V is found for PTB7-Th:IEICO-4F (Fig. S3), consistent with our estimate of ~60 mV extra losses from significant recombination *via* T_1.

In the blends presented here, we find the highest ΔV_{nr} values (≥0.35 V) in systems with large S_1-^{1}CTE offsets and recombination *via* T_1 (PM6:IT-4F, PBDB-T:ITIC, J51:ITIC, Table S1); due to the large S_1-^{1}CTE energy gap, thermal reactivation from ^{1}CTE to the bright NFA S_1 state is not efficient[17,42]. Consequently, the primary radiative pathway available is *via* the ^{1}CTE, where Φ_{PL} is ~100 times lower than the NFA S_1[17]. The smaller ΔV_{nr} (<0.35 V) blends are those with reduced S_1-^{1}CTE gaps. We note that in low offset systems, ΔV_{nr} is particularly sensitive to the S_1-^{1}CTE energy gap[17]. However, we can generally rationalise the observed ΔV_{nr} using Φ_{PL} for the NFA and the presence or absence of recombination *via* T_1. For example, both PM6:Y6 and PTB7-Th:IEICO-0F possess an S_1-^{1}CTE offset of ~50 meV (Fig. S63). However, despite the significantly lower Φ_{PL} (0.6%) for IEICO-0F compared to Y6 (1.3%), we report the lowest ΔV_{nr} =0.22 V in PTB7-Th:IEICO-0F (PM6:Y6 =0.25 V). Therefore, the improved ΔV_{nr} can be directly attributed to the suppressed recombination *via* T_1 in PTB7-Th:IEICO-0F.

To optimise power conversion efficiencies, we consider it of critical importance that OSCs are designed to avoid T_1 formation. We have therefore explored the role of D:A intermolecular interactions in T_1 generation through quantum-chemical calculations. Beginning with PTB7-Th:IEICO-2F, we have calculated the ^{1}CTE and ^{3}CTE energies at the equilibrium D:A geometry. We find the energy ordering of the CTEs is inverted from that expected when considering the electron exchange interaction[24], with the ^{3}CTE higher than the ^{1}CTE by ~70 meV. We next calculate the ^{1}CTE and ^{3}CTE excitation energies as a function of D:A separation. The results displayed in Fig. 3a show that below 0.5 nm, the ^{1}CTE is rapidly stabilised, whilst the ^{3}CTE is destabilised. In contrast, the explored PM6:Y6 configurations display the expected ordering with ^{1}CTE above ^{3}CTE (Figs. 3b and S66). By analysing the excited-state wavefunctions, we conclude that the inversion of ^{1}CTE and ^{3}CTE in PTB7-Th:IEICO-2F arises from hybridisation between the CTEs and local excitons (LEs)[11,18,19]. Inversion occurs because the NFA S_1 is higher in energy than the ^{1}CTE and the NFA T_1 is lower than the ^{3}CTE; hybridisation of these states therefore stabilises the ^{1}CTE and destabilises the ^{3}CTE (Fig. 3c). The primary reason for hybridisation is the enhanced electronic coupling in the PTB7-Th:IEICO-2F complex, due to: (i) the similar bonding-antibonding pattern of the highest-occupied molecular orbitals, with the same sequence of vertical nodal planes along the main molecular axis (Figs. 3d and S70); and (ii) the near-perfect registry between the NFA and the polymer backbone, offering significant molecular overlap (Fig. S65). The PM6 and Y6 combination does not possess these attributes and hence does not exhibit CTE:LE hybridisation. Additionally, we find excellent agreement between our calculations and experimental observations, with BCT T_1 formation only suppressed in the blends that exhibit significant CTE:LE hybridisation (Figs. 3a, 3b, S67).

The consequence of hybridisation destabilising the ^{3}CTE at close D:A separations is that it causes the electron and hole to remain more distant in the spin-triplet configuration, effectively increasing the interfacial ^{3}CTE radius. As the D:A electronic coupling, and thus k_{BCT}, falls exponentially with distance[48], this can provide additional time for the thermal re-dissociation of ^{3}CTE[49]. Our calculations of the CTE energies as a function of intermolecular separation for the PTB7-Th:IEICO-2F complex indicate that CTE:LE hybridisation results in a new ^{3}CTE energetic minima at a D:A stacking distance of 0.42 nm. When comparing k_{BCT} to the IEICO-2F T_1 at 0.42 nm to 0.35 nm, we observe that it is reduced by an order of magnitude from $\sim 10^{12}$ s^{-1} to $\sim 10^{11}$ s^{-1} (Fig. 3a). Consistent with our experimental observations where the NFA T_1 is populated *via* BCT, we also find that when the D polymer T_1 is energetically accessible from ^{3}CTE, k_{BCT} to the NFA is consistently higher (Fig. S64). Critically, the $k_{dissociation}$ of between 10^{10}-10^{11} s^{-1} that we observe experimentally in our NFA OSCs is comparable to the reduced k_{BCT} enabled by CTE:LE hybridisation, confirming that it is a feasible route to suppress BCT to T_1. We note that in thin films of organic semiconductors, there will be a range of intermolecular stacking distances (broadly centred around ~0.38 nm in conjugated polymers) due to disorder induced by the side chains[50]. Thus, in an operational OSC blend, our calculations suggest that the ^{3}CTE excitations will preferentially locate at lower energy interfacial sites with increased D:A stacking distances and reduced k_{BCT}.

From these observations, we offer design rules that encourage (triplet) CTE:LE hybridisation in OSC blends: (i) close energy resonance (preferably <100 meV) between the interacting LE and CTE states; (ii) strong overlap and phase matching between the interacting frontier molecular orbital wavefunctions of the D and A; and (iii) spatial registry between the D and A materials, allowing for the close intermolecular contacts necessary for strong wavefunction interactions.

Whilst the importance of optimising Φ_{PL} in OSCs is already well known[13], the insight provided by this work demonstrates the critical role of T_1 states in ΔE_{loss}. If T_1 formation can be suppressed, with ^{3}CTE-T_1 hybridisation providing one viable pathway, ΔE_{loss} can be reduced by ~60 meV; enough to enable PCEs of 20% with the current best device performance metrics[13,14]. Therefore, future OSC development should focus on simultaneously increasing Φ_{PL} and engineering-out T_1 formation. To achieve this, quantum chemical calculations on the D:A electronic interactions will provide a valuable predictive tool for screening perspective D:A pairs *in silico*. Furthermore, we anticipate the unprecedented spin-control over charge recombination demonstrated here will be of great interest to the broader field of excitonic semiconductors.

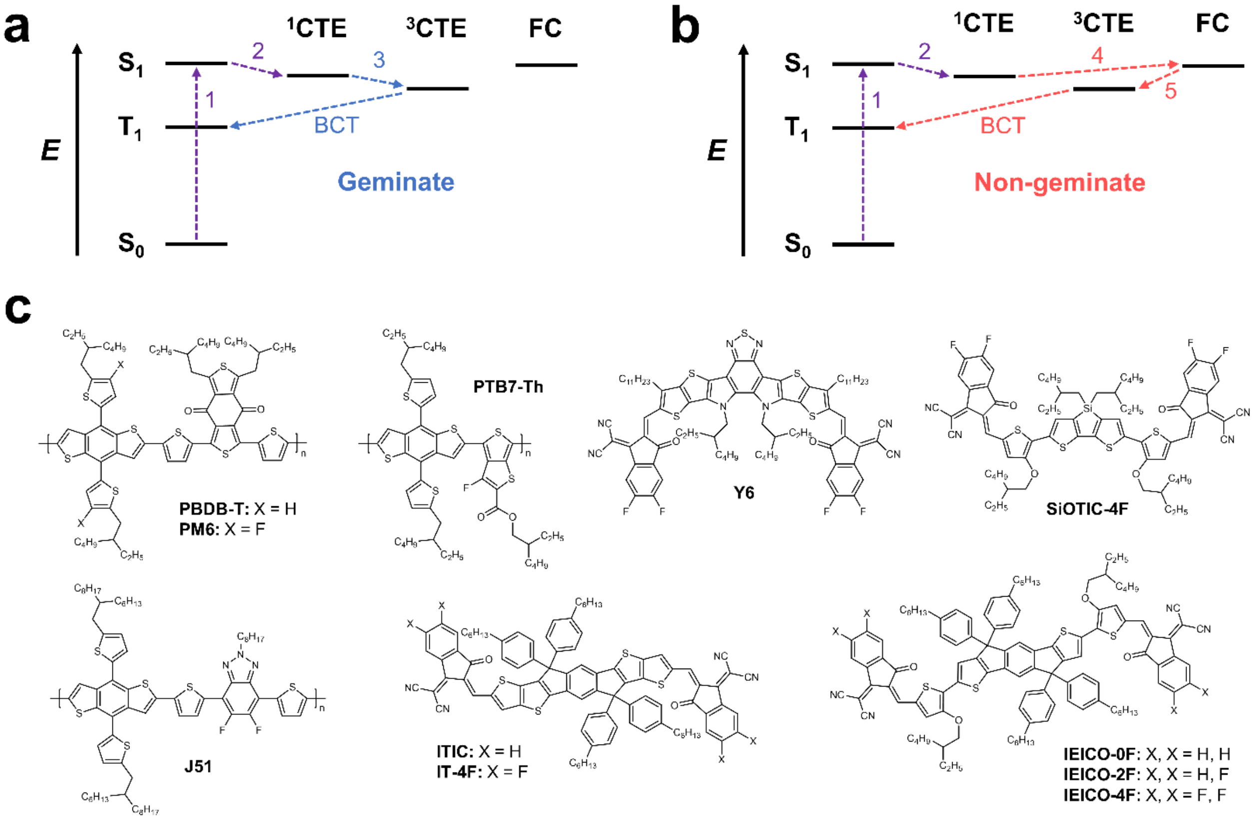

Figure 1: The triplet formation pathways and organic solar cell materials investigated in this study. (a) A diagram to illustrate the geminate pathway for T_1 formation in OSCs. After optical excitation (1), charge transfer from the S_1 to ^{1}CTE occurs (2). However, the ^{1}CTE does not manage to separate into FC before spin-mixing with the ^{3}CTE occurs on ns timescales (3). From the ^{3}CTE, BCT to a lower energy T_1 on either the D or A can occur. **(b)** A diagram to illustrate the non-geminate pathway for T_1 formation in OSCs. After optical excitation (1), charge transfer from the S_1 to ^{1}CTE occurs (2). The ^{1}CTE then successfully dissociates in FC (4). The FC then undergo non-geminate recombination, forming a 3:1 ratio of ^{3}CTE to ^{1}CTE (5). From the ^{3}CTE, BCT to a lower energy T_1 on either the D or A can occur. **(c)** The molecular structures of the four polymer donors and seven NFA materials used in this study.

Blend	PCE (%)	Φ_{PL} of NFA (%)	EQE$_{EL}$	ΔV_{nr} (V)	Geminate T_1	Non-geminate T_1
PM6:Y6	15.2	1.3	4.3 x 10^{-5}	0.25	No	Yes
PM6:IT-4F	12.0	1.4	9.5 x 10^{-7}	0.35	No	Yes
PM6:ITIC	9.2	1.4	5.0 x 10^{-5}	0.25	No	Yes
PBDB-T:ITIC	11.2	1.4	8.8 x 10^{-7}	0.35	No	Yes
J51:ITIC	7.2	1.4	7.1 x 10^{-8}	0.42	No	Yes
PTB7-Th: SiOTIC-4F	8.9	<0.1*	8.7 x 10^{-7}	0.35	No	Yes
PTB7-Th: IEICO-4F	10.2	0.4	1.6 x 10^{-6}	0.34	No	Yes
PTB7-Th: IEICO-2F	11.7	0.4	1.3 x 10^{-5}	0.28	No	No
PTB7-Th: IEICO-0F	7.2	0.6	1.4 x 10^{-4}	0.22	No	No

Table 1: A summary of the key parameters for the OSC blends investigated in this study. Φ_{PL} was measured for a neat film of the NFA used in the blend. The error in the Φ_{PL} is ±0.1%. *Φ_{PL} of SiOTIC-4F was too low to be measured and is therefore quoted as less than the smallest value reliably resolvable on our setup (0.1%). For the determination of ΔV_{nr}, the EQE$_{EL}$ at 293 K was taken at $-J_{SC}$ to ensure that carrier densities were relevant to device operating conditions. Additionally, it is stated whether the blend forms triplet excitons resulting from either geminate or non-geminate recombination pathways.

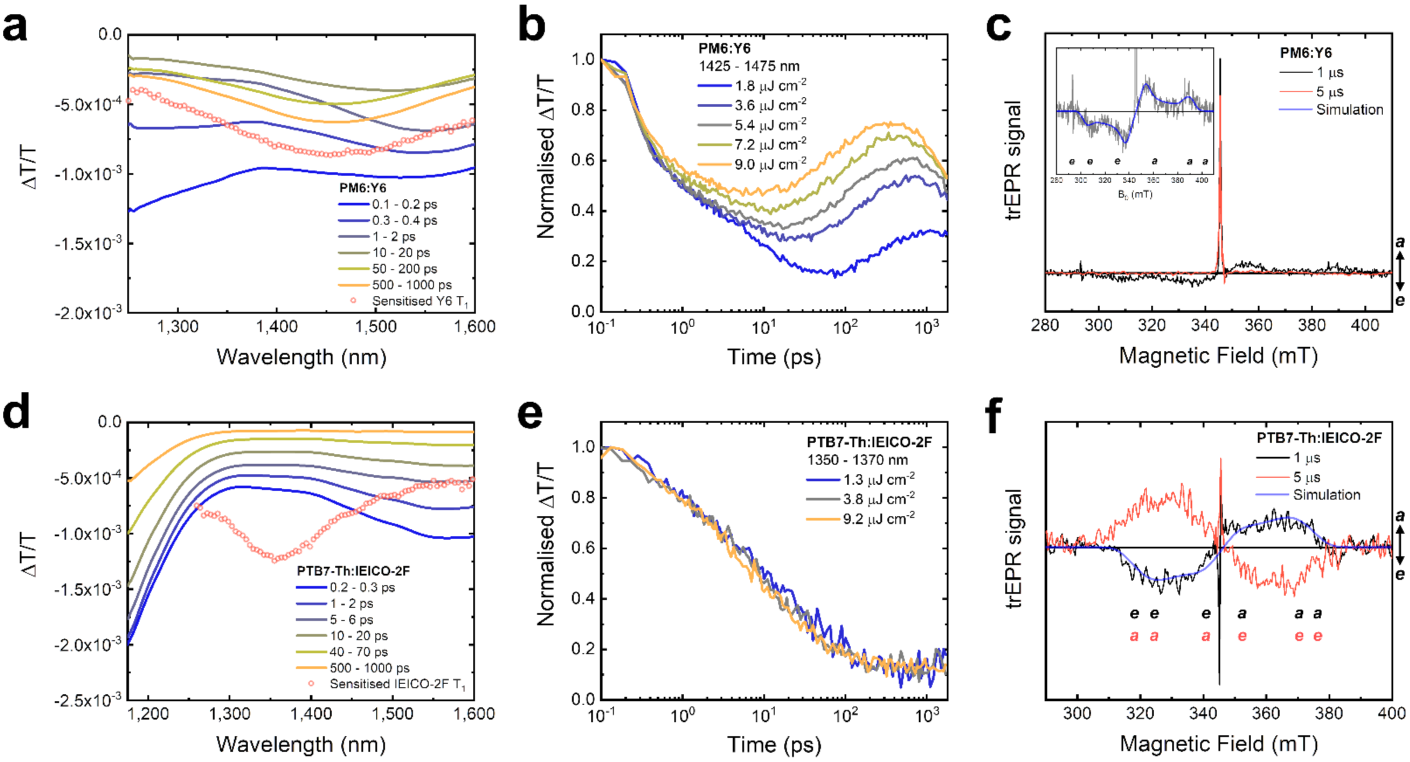

Figure 2: Spectroscopic investigations of triplet formation in model non-fullerene acceptor blends. (a) The IR region TA spectra of the PM6:Y6 blend (293 K), excited with a moderate fluence of 5.4 μJ cm^{-2} at 532 nm for preferential PM6 excitation. The Y6 T_1 PIA forms at 1450 nm, as confirmed by triplet sensitisation experiments. **(b)** The normalised TA kinetics of the PM6:Y6 blend, taken around the maximum of the Y6 T_1 feature between 1425 – 1475 nm. The clear fluence dependence of T_1 formation is indicative of a bimolecular generation pathway. **(c)** The trEPR spectra of the PM6:Y6 blend (80 K) after excitation at 532 nm, taken at 1 and 5 μs. The inset shows a magnification and simulation of the weak ISC triplet signal. The field positions of the absorption (*a*) and emission (*e*) EPR transitions of the ISC triplet are overlaid on the plot for clarity. **(d)** The IR region TA spectra of the PTB7-Th:IEICO-2F blend (293 K), excited with a moderate fluence of 3.8 μJ cm^{-2} at 620 nm for preferential PTB7-Th excitation. The IEICO-2F T_1 PIA at 1350 nm does not form in the blend. **(e)** The normalised TA kinetics of the PTB7-Th:IEICO-2F blend, taken around the maximum of the IEICO-2F T_1 PIA at 1350 – 1370 nm. No fluence dependence in the IEICO-2F T_1 region is observed. **(f)** The trEPR spectra of the PTB7-Th:IEICO-2F blend (80 K) after excitation at 532 nm, taken at 1 and 5 μs. The field positions of the absorption (*a*) and emission (*e*) EPR transitions of the ISC triplet are overlaid on the plot for clarity.

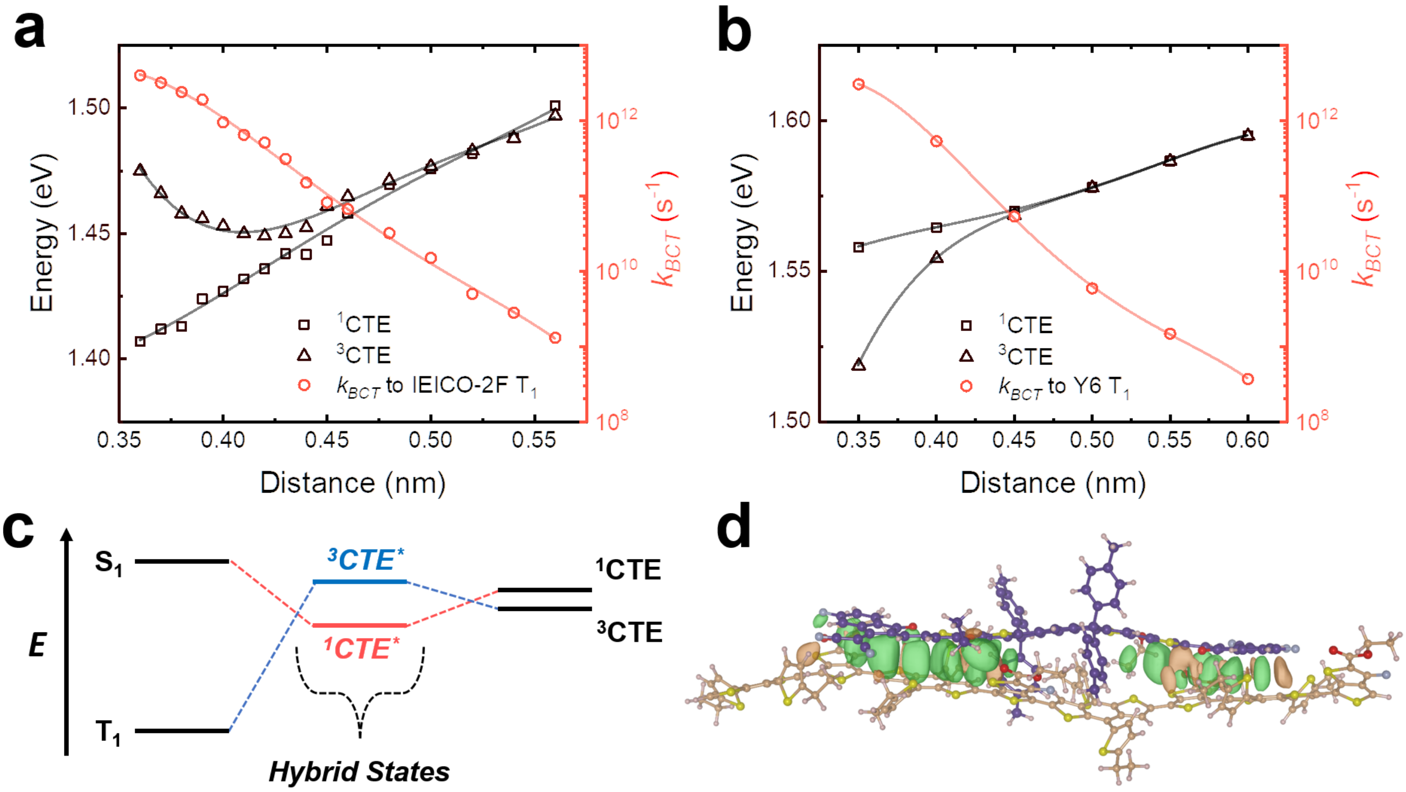

Figure 3: The role of hybridisation in organic solar cell blends. (a) The results of a rigid scan of the ^{1}CTE and ^{3}CTE energies for a representative PTB7-Th:IEICO-2F supramolecular configuration as a function of D:A separation. At each D:A separation, k_{BCT} from ^{3}CTE to T$_1$ of the NFA has also been calculated. The solid lines provide polynomial guides to the eye. **(b)** The results of a rigid scan of the ^{1}CTE and ^{3}CTE energies for a representative PM6:Y6 supramolecular configuration. At each D:A separation, k_{BCT} from ^{3}CTE to T$_1$ of the NFA has also been calculated. The solid lines provide polynomial guides to the eye. **(c)** A schematic to represent the effect of CTE-LE hybridisation on the energetic ordering of the ^{1}CTE and ^{3}CTE. **(d)** An image showing the same optimised supramolecular configuration between PTB7-Th (beige) IEICO-2F (purple) used for the calculations in Fig. 3a. The lobes represent regions of constructive overlap between the highest-occupied molecular orbitals (HOMOs) of D and A. The HOMO overlap that controls the size of the electronic coupling and thus mediates hybridisation between the NFA LE and the CTEs; for hybridisation between the LE states of the D polymer and the CTEs, the lowest occupied molecular orbital overlap is the relevant interaction.

Methods

Rate equations for the processes controlling triplet formation in OSC blends

In the event that BCT proceeds to the electron acceptor, k_{BCT} and $k_{dissociation}$ can be defined as[51]:

$$^{3}[D^{+}][A^{-}] \xrightarrow{k_{BCT}} {}_{0}^{1}[D] + {}_{1}^{3}[A] \tag{3}$$

$$^{3}[D^{+}][A^{-}] \xrightarrow{k_{dissociation}} [D^{+}] + [A^{-}] \tag{4}$$

Where $[D^{+}]$ is the free hole on the donor component, $[A^{-}]$ is the free electron on the acceptor material, $^{3}[D^{+}][A^{-}]$ represents the coulombically-bound ^{3}CTE, ${}_{0}^{1}[D]$ is the spin-singlet ground state of the donor and ${}_{1}^{3}[A]$ is T_1 of the acceptor. We note that the conversion of ^{3}CTE back into ^{1}CTE primarily occurs via hyperfine coupling (HFC), typically taking place with a rate of 10^{8}-10^{6} s^{-1} in organic semiconductors[27]; we note that this is significantly slower than the k_{BCT} and $k_{dissociation}$ determined in our work, which are both on the order of 10^{10}-10^{12} s^{-1}. The rate of the HFC-induced ^{3}CTE-^{1}CTE interconversion process (k_{HFC}) is given by:

$$^{3}[D^{+}][A^{-}] \xrightarrow{k_{HFC}} {}^{1}[D^{+}][A^{-}] \tag{5}$$

Where $^{1}[D^{+}][A^{-}]$ represents the coulombically-bound ^{1}CTE. In addition to the primary geminate and non-geminate pathways occurring via CTEs that are discussed in our work, T_1 formation via direct SOC-ISC from un-dissociated S_1 states can also be considered a geminate T_1 formation mechanism and is the only geminate pathway detected in the trEPR measurements of our NFA blends. However, as it requires S_1 to remain undissociated, it will not be a significant pathway in blends that exhibit efficient exciton dissociation and good device performance. The rate of intersystem crossing (k_{ISC}) from S_1 to T_1, defined here for the acceptor component, is given by:

$$ {}^{1}_{1}[A] \xrightarrow{k_{ISC}} + {}^{3}_{1}[A] \tag{6} $$

Where ${}^{1}_{1}[A]$ is S_1 of the acceptor.

OSC device fabrication

Indium tin oxide (ITO) patterned glass substrates were cleaned by scrubbing with soapy water, followed by sonication in soapy water, deionized (DI) water, acetone, and isopropanol for 20 minutes each. The substrates were dried using compressed nitrogen and placed in an oven overnight at 100 °C. The conventional architecture devices were made by treating the ITO substrates with UV-ozone for 15 minutes and spin-coating a layer of poly(3,4-ethylenedioxythiophene):poly(styrenesulfonate) (PEDOT:PSS, Clevios P VP Al 8043) at 3000 rpm for 40 s onto the ITO substrates in air. The substrates were then annealed in air at 150 °C for 20 minutes. Active layers were spin coated on top of the PEDOT:PSS layer inside a nitrogen filled glovebox following the recipes from previous reports[9,42,52]. The substrates were then pumped down under vacuum ($<10^{-7}$ torr), and a 5 nm thick Ca interlayer followed by a 100 nm thick Al electrode were deposited on top of the active layer by thermal evaporation using the Angstrom Engineering Series EQ Thermal Evaporator. In the case of inverted architecture devices, ZnO was used as the bottom transparent electrode (replacing PEDOT:PSS), where the ZnO solution was prepared in a nitrogen glovebox by mixing tetrahydrofuran and diethylzinc (2:1). The fresh ZnO solution was then spin-coated atop the clean ITO substrates at 4000 rpm for 30 seconds and then placed on a hotplate at 110 ^{0}C for 15 minutes. Following active layer spin-coating, the inverted devices were pumped down under vacuum ($<10^{-7}$ torr), and 7 nm of MoO_x and 100 nm thick Ag electrode were deposited on top of the active layer by thermal evaporation. The electrode overlap area was 0.22 cm^2 for both conventional and inverted devices. The active area of the device was determined using an optical microscope. The optimized active layer compositions used for the blend solutions were based on previously published reports[9,42,52].

OSC device testing

Photovoltaic characteristic measurements were carried out inside a N_2 filled glove box. Solar-cell device properties were measured under illumination by a simulated 100 mW cm^{-2} AM1.5 G light source using a 300 W Xe arc lamp with an AM 1.5 global filter. The irradiance was adjusted to 1 sun with a standard silicon photovoltaic cell calibrated by the National Renewable Energy Laboratory. No spectral mismatch correction was applied. A Keithley 2635A source measurement unit was used to scan the voltage applied to the solar cell between -2 to 1 V at a speed of 0.43 V/s with a dwell time of 46 ms. Scans were performed in both the forward and reverse directions, with no unusual behaviour observed. Between eight and 30 individual solar cell devices were tested for each blend reported. The error associated with the reported PCE values is ±0.2%.

Electroluminescence and EQE_{EL} measurements

EL measurements were performed using two setups depending on the wavelength range of interest. For measurements under 1050 nm, a home-made EL spectrometer was used. The EL emission from a sample driven by a Keithley source-measure unit (model 2602A) was collected by a lens system and focused on the entrance slit of a spectrograph (Acton Research SP-500) equipped with a Si charge-coupled detector (Princeton Instruments Pixis:400). The spectra collected by the detector were corrected for the instrument response function. The correction factors were determined by measuring the spectrum of a black body-like light source (Ocean Optics LS-1). For EL measurements in the range 900 - 1700 nm, we utilized a Photon Technology International (PTI) Quantamaster fluorimeter equipped with an Edinburgh Instruments EI-L Ge detector. The excitation monochromator of the fluorimeter was not used, and the EL emission was generated by driving the devices by a Keithley 2602 source-measure unit. An optical chopper (Thorlabs MC2000) was placed in front of the emission monochromator to make use of the fluorimeter's lock-in amplifier-based detection system. The PTI Felix fluorimeter software was used for the data collection and correction of the instrumental artefacts. The efficiency of EL was obtained by applying a bias from -1 to 2V with a dual-channel Keithley 2602 to the solar cell and placing a silicon or germanium photodiode directly in front of it to collect the emission as a function of applied bias. The current running through the device and the photodiode were simultaneously measured.

Photoluminescence quantum efficiency measurements

The PLQE was determined using method previously described by De Mello *et al.*[53]. Samples were placed in an integrating sphere and photoexcited using a 658 nm continuous-wave laser. The laser and emission signals were measured and quantified using calibrated Andor iDus DU420A BVF Si and Andor CCD-1430 InGaAs detectors.

TA spectroscopy

In TA, T_1 states often possess distinct PIA features, allowing for their unambiguous assignment. Furthermore, by investigating the fluence dependence of the T_1 dynamics, we can readily determine whether formation follows the bimolecular kinetics expected for NGR[22], or the monomolecular kinetics anticipated if T_1 is produced from geminate processes[29]. We can also quantify the T_1 population (N_T) directly from the TA signal through knowledge of the T_1 absorption cross section (σ_T), corresponding to the TA signal produced by a single T_1 state[54] (see SI for more details).

$$\frac{\Delta T}{T} = \sigma_T N_T \tag{7}$$

Samples for TA measurements were fabricated by spin-coating solutions onto quartz substrates using identical conditions to the optimised devices. The samples were encapsulated in a nitrogen glovebox environment to ensure oxygen-free measurements.

TA was performed on either one of two experimental setups. The broadband probe (525 – 1650 nm) TA was performed on a setup powered using a commercially available Ti:sapphire amplifier (Spectra Physics Solstice Ace). The amplifier operates at 1 kHz and generates 100 fs pulses centred at 800 nm with an output of 7 W. A TOPAS optical parametric amplifier (OPA) was used to provide the tuneable ~100 fs pump pulses for the “short-time” (100 fs – 1.8 ns) TA measurements, whilst the second harmonic (532 nm) of an electronically triggered, Q-switched Nd:YVO_4 laser (Advanced Optical Technologies Ltd AOT-YVO-25QSPX) provided the ~1 ns pump pulses for the “long-time” (1 ns – 100 μs) TA measurements. The probe was provided by a broadband visible (525 – 775 nm), NIR (800 – 1200 nm) and IR (1250 – 1650 nm) NOPAs. The probe pulses are collected with an InGaAs dual-line array detector (Hamamatsu G11608-512DA), driven and read out by a custom-built board from Stresing Entwicklungsbüro. The probe beam was split into two identical beams by a 50/50 beamsplitter. This allowed for the use of a second reference beam which also passes through the sample but does not interact with the pump. The role of the reference was to correct for any shot-to-shot fluctuations in the probe that would otherwise greatly increase the structured noise in our experiments. Through this arrangement, very small signals with a $\frac{\Delta T}{T}$ =1x10^{-5} could be measured.

For the 500 – 950 nm continuous probe region TA, a Yb amplifier (PHAROS, Light Conversion), operating at 38 kHz and generating 200 fs pulses centred at 1030 nm with an output of 14.5 W was used. The ~200 fs pump pulse was provided by a TOPAS OPA. The probe is provided by a white light supercontinuum generated in a YAG crystal from a small amount of the 1030 nm fundamental. After passing through the sample, the probe is imaged using a Si photodiode array (Stresing S11490). This setup provided additional flexibility by allowing for broadband spectrum acquisition in one measurement, as well good signal to noise in the 750 – 850 nm region, which is difficult to obtain on the other setup due to large fluctuations in the NOPA probes around the 800 nm fundamental of the Ti:sapphire laser.

In our TA measurements on the PM6:Y6 blend, the excitation densities created by our 1.8 μJ cm^{-2} pulse at 532 nm is equivalent to “3 sun” operation conditions for PM6:Y6 (~3x10^{17} cm^{-3})[42]. In contrast, the 9.0 μJ cm^{-2} pulse at 532 nm is equivalent to “15 sun” operation. We have intentionally performed our TA measurements at excitation densities in excess of those at “1 sun”, as the increased rate of non-geminate recombination enables us to identify and model the triplet recombination pathways present in the OSC blends studied here. We note that under “1 sun” conditions, the lower excitation densities will increase the time taken to the onset of non-geminate recombination processes that result in T_1 formation, enabling charge carriers to be extracted before significant recombination losses to T_1 occur. This can explain why the PM6:Y6 devices investigated here (which have shown particularly efficient charge extraction[42]) can demonstrate excellent performance, despite 90% of recombination proceeding *via* the Y6 T_1 under open-circuit conditions.

trEPR spectroscopy

Triplet states can also be investigated using trEPR measurements, which allows for the detection of only spin-polarised triplets i.e. those where the spin sublevels T_+, T_0 and T_- have non-thermal occupancies[44]. As a result, we observe enhanced absorptive (*a*) and emissive (*e*) characters of the EPR transitions, from which the generation mechanism of the triplet can be determined[44]. Triplets produced via non-geminate recombination from FC have thermal sublevel occupancies and are thus not detectable[20]. Conversely, triplets produced from geminate processes result in sublevel occupancies far from thermal equilibrium and can be readily observed[23,44,45,55–57]. T_1 formation via geminate BCT can be understood in the framework of the spin-correlated radical pair mechanism[58–61], where spin-mixing first occurs between $^1CTE_0$ and $^3CTE_0$, followed by BCT to the molecular triplet sublevels. Depending on the sign of the zero-field splitting D-parameter, the overpopulation of either T_0 or T_+/T_- results in an *aeeaae* or *eaaeea* spin-polarization pattern of the T_1 trEPR signal; a clear and unique fingerprint of the geminate pathway[23,44,45]. Though performed at 80 K, we expect that these measurements are of relevance to the blend behaviour at 293 K; detailed discussions of the influence of temperature and an in-depth review of EPR theory are available in the SI.

EPR samples were fabricated by spin-coating solutions under identical conditions to the optimised devices onto Mylar substrates, which were subsequently cut into strips with a width of 3 mm. To ensure the flexible Mylar substrates did not bend during the spin coating process, they were mounted onto rigid glass substrates using adhesive tape. The strips were placed in quartz EPR tubes which were sealed in a nitrogen glovebox with a bi-component resin (Devcon 5-Minute Epoxy), ensuring that all EPR measurements were performed without oxygen exposure.

All trEPR spectra were recorded on a Bruker Elexsys E580 X-band spectrometer, equipped with a nitrogen gas-flow cryostat for sample temperature control. The sample temperature was maintained with an Oxford Instruments CF935O cryostat and controlled with an Oxford Instruments ITC503. Laser pulses for trEPR were collimated into the cryostat and resonator windows from a multi-mode optical fibre, ThorLabs FT600UMT. Sample excitation at 532 nm with an energy of 2 mJ per pulse and a duration of 7 ns was provided by the residual 2nd harmonic output of a Newport/Spectra Physics Lab 170 Quanta Ray Nd:YAG pulsed laser, operating at 20 Hz. The trEPR signal was recorded through a Bruker SpecJet II transient recorder with timing synchronisation by a Stanford Research Systems DG645 delay generator. The instrument response time was about 200 ns. The spectra were acquired with 2 mW microwave power and averaging 400 transient signals at each field position.

The trEPR spectra were recorded by adopting a direct-detection scheme[62]. Specifically, the EPR intensity was recorded as a function of time following laser excitation, with constant applied X-band microwave radiation, for each magnetic field position. We employed this configuration since it possesses better signal-to-noise ratio compared to the delay after flash (DAF) echo-detected experiments at 80 K. Indeed, most triplet states have relaxation times too short to be detectable with pulsed-detection scheme at 80 K. At lower temperatures (usually 20 K), pulsed detection usually becomes feasible, but the spectra may become quite complicated due to several paramagnetic species being present, including thermally populated triplets produced via non-geminate recombination from free charge carriers and stable states that are not usually observable using direct detection. From the data set obtained, the transient EPR spectrum at different time delays after the laser pulse has been extracted. The reported trEPR spectra have been averaged over a time window of 1 μs. The acquired trEPR spectra have been simulated by using the core functions *pepper* and *esfit* of the open-source MATLAB toolbox

EasySpin[63]. The parameters included in our best-fit simulations are the ZFS parameters (D and E), the triplet population sublevels (p_1, p_2, p_3) and the line broadening (assumed as only Lorentzian to not over-parametrize the fitting). For the calculation of spin polarization, the populations of the spin-triplet sublevels at zero field were calculated (T_x, T_y, T_z) in the fitting program and used by EasySpin to simulate the trEPR spectrum at resonant fields. For all the simulations, the g tensor was assumed isotropic with g_{iso}=2.002. To carry out our least-square fittings, a user-defined simulation function has been developed which allowed the fitting of “non-spin system” parameters, such as the spin populations of the triplet sublevels. All the fits were carried out using a Nelder/Mead downhill simplex optimisation algorithm.

Acknowledgements

A.J.G. and R.H.F. acknowledge support from the Simons Foundation (grant no. 601946) and the EPSRC (EP/M01083X/1 and EP/M005143/1). This project has received funding from the ERC under the European Union’s Horizon 2020 research and innovation programme (grant agreement no. 670405). A.K. and T.-Q.N. were supported by the Department of the Navy, Office of Naval Research Award No. N00014-14-1-0580. A.K. acknowledges funding by the Schlumberger foundation. A.Privitera, R.D., A.Pershin, G.L., M.K.R. and D.B. were supported by the European Union's Horizon 2020 research and innovation programme under Marie Sklodowska Curie Grant agreement No.722651 (SEPOMO project). Computational resources in Mons were provided by the Consortium des Équipements de Calcul Intensif (CÉCI), funded by the Fonds de la Recherche Scientifiques de Belgique (F.R.S.-FNRS) under Grant No. 2.5020.11, as well as the Tier-1 supercomputer of the Fedération Wallonie-Bruxelles, infrastructure funded by the Walloon Region under Grant Agreement No. 1117545. D.B. is a FNRS Research Director. F.G. acknowledges the Stiftelsen för Strategisk Forskning through a Future Research Leader program (FFL18-0322). trEPR measurements were performed in the

Centre for Advanced ESR (CAESR) located in the Department of Chemistry of the University of Oxford, and this work was supported by the EPSRC (EP/L011972/1). We thank Till Biskup and Andreas Sperlich for their assistance with the simulation and interpretation of the trEPR data presented in this work.

Author contributions

A.J.G., T.-Q.N. and R.H.F. conceived the work. A.J.G. performed the TA measurements. A.Privitera and W.K.M. conducted the trEPR measurements. R.D., A.Pershin and G.L. carried out the quantum chemical calculations. A.K., D.Q., J.Y. and S.-J.K. fabricated and tested the OSC devices. A.J.G. and J.Y. performed the PLQE measurements. J.L. synthesised SiOTIC-4F and the IEICO derivatives. M.K.R., F.G., G.C.B., T.-Q.N, D.B. and R.H.F. supervised their group members involved in the project. A.J.G., A.R. and R.H.F. wrote the manuscript with input from all authors.

Competing financial interests

The authors declare no competing interests.

Additional information

Supplementary information accompanies this paper at [to be completed in proofs].

Correspondence and requests for materials should be addressed to R.H.F. (rhf10@cam.ac.uk), A.J.G. (ajg216@cam.ac.uk), D.B. (david.beljonne@umons.ac.be) and T.-Q.N. (quyen@chem.ucsb.edu).

Reprints and permissions information is available at www.nature.com/reprints.

Data availability

The data that supports the findings of this study are available from the corresponding authors upon reasonable request.

Bibliography

1. Liu, Q. *et al.* 18% Efficiency organic solar cells. *Sci. Bull.* **65**, 272–275 (2020).
2. Green, M. A. *et al.* Solar cell efficiency tables (Version 55). *Prog. Photovoltaics Res. Appl.* **28**, 3–15 (2020).
3. Liu, S. *et al.* High-efficiency organic solar cells with low non-radiative recombination loss and low energetic disorder. *Nat. Photonics* **14**, 300–305 (2020).
4. Menke, S. M., Ran, N. A., Bazan, G. C. & Friend, R. H. Understanding Energy Loss in Organic Solar Cells: Toward a New Efficiency Regime. *Joule* **2**, 25–35 (2018).
5. Yuan, J. *et al.* Single-Junction Organic Solar Cell with over 15% Efficiency Using Fused-Ring Acceptor with Electron-Deficient Core. *Joule* **3**, 1140–1151 (2019).
6. Shockley, W. & Queisser, H. J. Detailed Balance Limit of Efficiency of p-n Junction Solar Cells. *J. Appl. Phys.* **32**, 510–519 (1961).
7. Ross, R. T. Some Thermodynamics of Photochemical Systems. *J. Chem. Phys.* **46**, 4590–4593 (1967).
8. Rau, U. Reciprocity relation between photovoltaic quantum efficiency and electroluminescent emission of solar cells. *Phys. Rev. B* **76**, 085303 (2007).

9. Lee, J. *et al.* Design of Nonfullerene Acceptors with Near-Infrared Light Absorption Capabilities. *Adv. Energy Mater.* **8**, 1801209 (2018).

10. Cui, Y. *et al.* Over 16% efficiency organic photovoltaic cells enabled by a chlorinated acceptor with increased open-circuit voltages. *Nat. Commun.* **10**, 2515 (2019).

11. Qian, D. *et al.* Design rules for minimizing voltage losses in high-efficiency organic solar cells. *Nat. Mater.* **17**, 703–709 (2018).

12. Zhou, Z. *et al.* Subtle Molecular Tailoring Induces Significant Morphology Optimization Enabling over 16% Efficiency Organic Solar Cells with Efficient Charge Generation. *Adv. Mater.* **32**, 1906324 (2020).

13. Li, S., Li, C., Shi, M. & Chen, H. New Phase for Organic Solar Cell Research: Emergence of Y-Series Electron Acceptors and Their Perspectives. *ACS Energy Lett.* **5**, 1554–1567 (2020).

14. Yuan, J. *et al.* Reducing Voltage Losses in the A-DA′D-A Acceptor-Based Organic Solar Cells. *Chem* **6**, 2147–2161 (2020).

15. Vandewal, K., Mertens, S., Benduhn, J. & Liu, Q. The Cost of Converting Excitons into Free Charge Carriers in Organic Solar Cells. *J. Phys. Chem. Lett.* **11**, 129–135 (2020).

16. Geffroy, B., le Roy, P. & Prat, C. Organic light-emitting diode (OLED) technology: Materials, devices and display technologies. *Polym. Int.* **55**, 572–582 (2006).

17. Classen, A. *et al.* The role of exciton lifetime for charge generation in organic solar cells at negligible energy-level offsets. *Nat. Energy* **5**, 711–719 (2020).

18. Eisner, F. D. *et al.* Hybridization of Local Exciton and Charge-Transfer States Reduces Nonradiative Voltage Losses in Organic Solar Cells. *J. Am. Chem. Soc.* **141**, 6362–

6374 (2019).

19. Chen, X.-K., Coropceanu, V. & Brédas, J.-L. Assessing the nature of the charge-transfer electronic states in organic solar cells. *Nat. Commun.* **9**, 5295 (2018).

20. Wang, J., Chepelianskii, A., Gao, F. & Greenham, N. C. Control of exciton spin statistics through spin polarization in organic optoelectronic devices. *Nat. Commun.* **3**, 1191 (2012).

21. Chen, X.-K., Wang, T. & Brédas, J.-L. Suppressing Energy Loss due to Triplet Exciton Formation in Organic Solar Cells: The Role of Chemical Structures and Molecular Packing. *Adv. Energy Mater.* **7**, 1602713 (2017).

22. Rao, A. *et al.* The role of spin in the kinetic control of recombination in organic photovoltaics. *Nature* **500**, 435–439 (2013).

23. Kraffert, F. *et al.* Charge Separation in PCPDTBT:PCBM Blends from an EPR Perspective. *J. Phys. Chem. C* **118**, 28482–28493 (2014).

24. Köhler, A. & Beljonne, D. The Singlet–Triplet Exchange Energy in Conjugated Polymers. *Adv. Funct. Mater.* **14**, 11–18 (2004).

25. Hodgkiss, J. M. *et al.* Exciton-Charge Annihilation in Organic Semiconductor Films. *Adv. Funct. Mater.* **22**, 1567–1577 (2012).

26. Benduhn, J. *et al.* Impact of Triplet Excited States on the Open-Circuit Voltage of Organic Solar Cells. *Adv. Energy Mater.* **8**, 1800451 (2018).

27. Cohen, A. E. Nanomagnetic Control of Intersystem Crossing. *J. Phys. Chem. A* **113**, 11084–11092 (2009).

28. Shoaee, S. *et al.* Decoding Charge Recombination through Charge Generation in

Organic Solar Cells. *Sol. RRL* **3**, 1900184 (2019).

29. Dimitrov, S. D. *et al.* Polaron pair mediated triplet generation in polymer/fullerene blends. *Nat. Commun.* **6**, 6501 (2015).

30. Salvadori, E. *et al.* Ultra-fast spin-mixing in a diketopyrrolopyrrole monomer/fullerene blend charge transfer state. *J. Mater. Chem. A* **5**, 24335–24343 (2017).

31. Menke, S. M. *et al.* Limits for Recombination in a Low Energy Loss Organic Heterojunction. *ACS Nano* **10**, 10736–10744 (2016).

32. Xue, L. *et al.* Side Chain Engineering on Medium Bandgap Copolymers to Suppress Triplet Formation for High-Efficiency Polymer Solar Cells. *Adv. Mater.* **29**, 1703344 (2017).

33. Chow, P. C. Y., Gélinas, S., Rao, A. & Friend, R. H. Quantitative bimolecular recombination in organic photovoltaics through triplet exciton formation. *J. Am. Chem. Soc.* **136**, 3424–3429 (2014).

34. Di Nuzzo, D. *et al.* Improved Film Morphology Reduces Charge Carrier Recombination into the Triplet Excited State in a Small Bandgap Polymer-Fullerene Photovoltaic Cell. *Adv. Mater.* **22**, 4321–4324 (2010).

35. Karuthedath, S. *et al.* Buildup of Triplet-State Population in Operating TQ1:PC 71 BM Devices Does Not Limit Their Performance. *J. Phys. Chem. Lett.* **11**, 2838–2845 (2020).

36. Wang, R. *et al.* Charge Separation from an Intra-Moiety Intermediate State in the High-Performance PM6:Y6 Organic Photovoltaic Blend. *J. Am. Chem. Soc.* **142**, 12751–12759 (2020).

37. Gelinas, S. *et al.* Ultrafast Long-Range Charge Separation in Organic Semiconductor

Photovoltaic Diodes. *Science (80-.).* **343**, 512–516 (2014).

38. Jakowetz, A. C. *et al.* Visualizing excitations at buried heterojunctions in organic semiconductor blends. *Nat. Mater.* **16**, 551–557 (2017).

39. Menke, S. M. *et al.* Order enables efficient electron-hole separation at an organic heterojunction with a small energy loss. *Nat. Commun.* **9**, 277 (2018).

40. Burke, T. M., Sweetnam, S., Vandewal, K. & McGehee, M. D. Beyond Langevin Recombination: How Equilibrium Between Free Carriers and Charge Transfer States Determines the Open-Circuit Voltage of Organic Solar Cells. *Adv. Energy Mater.* **5**, 1500123 (2015).

41. Hosseini, S. M. *et al.* Putting Order into PM6:Y6 Solar Cells to Reduce the Langevin Recombination in 400 nm Thick Junction. *Sol. RRL* **4**, 2000498 (2020).

42. Karki, A. *et al.* Understanding the High Performance of over 15% Efficiency in Single-Junction Bulk Heterojunction Organic Solar Cells. *Adv. Mater.* **31**, 1903868 (2019).

43. Niklas, J. *et al.* Highly-efficient charge separation and polaron delocalization in polymer–fullerene bulk-heterojunctions: a comparative multi-frequency EPR and DFT study. *Phys. Chem. Chem. Phys.* **15**, 9562 (2013).

44. Richert, S., Tait, C. E. & Timmel, C. R. Delocalisation of photoexcited triplet states probed by transient EPR and hyperfine spectroscopy. *J. Magn. Reson.* **280**, 103–116 (2017).

45. Thomson, S. A. J. *et al.* Charge Separation and Triplet Exciton Formation Pathways in Small-Molecule Solar Cells as Studied by Time-Resolved EPR Spectroscopy. *J. Phys. Chem. C* **121**, 22707–22719 (2017).

46. Hintze, C., Steiner, U. E. & Drescher, M. Photoexcited Triplet State Kinetics Studied by Electron Paramagnetic Resonance Spectroscopy. *ChemPhysChem* **18**, 6–16 (2017).

47. Benduhn, J. *et al.* Intrinsic non-radiative voltage losses in fullerene-based organic solar cells. *Nat. Energy* **2**, 17053 (2017).

48. Kubas, A. *et al.* Electronic couplings for molecular charge transfer: benchmarking CDFT, FODFT and FODFTB against high-level ab initio calculations. II. *Phys. Chem. Chem. Phys.* **17**, 14342–14354 (2015).

49. Chang, W. *et al.* Spin-dependent charge transfer state design rules in organic photovoltaics. *Nat. Commun.* **6**, 6415 (2015).

50. Street, R. A., Song, K. W., Northrup, J. E. & Cowan, S. Photoconductivity measurements of the electronic structure of organic solar cells. *Phys. Rev. B* **83**, 165207 (2011).

51. Rasaiah, J. C., Hubbard, J. B., Rubin, R. J. & Lee, S. H. Kinetics of bimolecular recombination processes with trapping. *J. Phys. Chem.* **94**, 652–662 (1990).

52. Lee, J. *et al.* Bandgap Narrowing in Non-Fullerene Acceptors: Single Atom Substitution Leads to High Optoelectronic Response Beyond 1000 nm. *Adv. Energy Mater.* **8**, 1801212 (2018).

53. de Mello, J. C., Wittmann, H. F. & Friend, R. H. An improved experimental determination of external photoluminescence quantum efficiency. *Adv. Mater.* **9**, 230–232 (1997).

54. Lee, C.-L., Yang, X. & Greenham, N. C. Determination of the triplet excited-state absorption cross section in a polyfluorene by energy transfer from a phosphorescent metal complex. *Phys. Rev. B* **76**, 245201 (2007).

55. Biskup, T. Structure–Function Relationship of Organic Semiconductors: Detailed Insights From Time-Resolved EPR Spectroscopy. *Front. Chem.* **7**, (2019).

56. Weber, S. Transient EPR. in *eMagRes* 255–270 (John Wiley & Sons, Ltd, 2017). doi:10.1002/9780470034590.emrstm1509

57. Niklas, J. & Poluektov, O. G. Charge Transfer Processes in OPV Materials as Revealed by EPR Spectroscopy. *Adv. Energy Mater.* **7**, 1602226 (2017).

58. Righetto, M. *et al.* Engineering interactions in QDs–PCBM blends: a surface chemistry approach. *Nanoscale* **10**, 11913–11922 (2018).

59. Franco, L. *et al.* Time-Resolved EPR of Photoinduced Excited States in a Semiconducting Polymer/PCBM Blend. *J. Phys. Chem. C* **117**, 1554–1560 (2013).

60. Buckley, C. D., Hunter, D. A., Hore, P. J. & McLauchlan, K. A. Electron spin resonance of spin-correlated radical pairs. *Chem. Phys. Lett.* **135**, 307–312 (1987).

61. Hore, P. J., Hunter, D. A., McKie, C. D. & Hoff, A. J. Electron paramagnetic resonance of spin-correlated radical pairs in photosynthetic reactions. *Chem. Phys. Lett.* **137**, 495–500 (1987).

62. Biskup, T. Structure–Function Relationship of Organic Semiconductors: Detailed Insights From Time-Resolved EPR Spectroscopy. *Front. Chem.* **7**, 1–22 (2019).

63. Stoll, S. & Schweiger, A. EasySpin, a comprehensive software package for spectral simulation and analysis in EPR. *J. Magn. Reson.* **178**, 42–55 (2006).

Figure Legends

Figure 1: The triplet formation pathways and organic solar cell materials investigated in this study. (a) A diagram to illustrate the geminate pathway for T_1 formation in OSCs. After optical excitation (1), charge transfer from the S_1 to ^{1}CTE occurs (2). However, the ^{1}CTE does not manage to separate into FC before spin-mixing with the ^{3}CTE occurs on ns timescales (3). From the ^{3}CTE, BCT to a lower energy T_1 on either the D or A can occur. **(b)** A diagram to illustrate the non-geminate pathway for T_1 formation in OSCs. After optical excitation (1), charge transfer from the S_1 to ^{1}CTE occurs (2). The ^{1}CTE then successfully dissociates in FC (4). The FC then undergo non-geminate recombination, forming a 3:1 ratio of ^{3}CTE to ^{1}CTE (5). From the ^{3}CTE, BCT to a lower energy T_1 on either the D or A can occur. **(c)** The molecular structures of the four polymer donors and seven NFA materials used in this study.

Table 1: A summary of the key parameters for the OSC blends investigated in this study. Φ_{PL} was measured for a neat film of the NFA used in the blend. The error in the Φ_{PL} is ±0.1%. *Φ_{PL} of SiOTIC-4F was too low to be measured and is therefore quoted as less than the smallest value reliably resolvable on our setup (0.1%). For the determination of ΔV_{nr}, the EQE_{EL} at 293 K was taken at $-J_{SC}$ to ensure that carrier densities were relevant to device operating conditions. Additionally, it is stated whether the blend forms triplet excitons resulting from either geminate or non-geminate recombination pathways.

Figure 2: Spectroscopic investigations of triplet formation in model non-fullerene acceptor blends. (a) The IR region TA spectra of the PM6:Y6 blend (293 K), excited with a moderate fluence of 5.4 μJ cm^{-2} at 532 nm for preferential PM6 excitation. The Y6 T_1 PIA forms at 1450 nm, as confirmed by triplet sensitisation experiments. **(b)** The normalised TA

kinetics of the PM6:Y6 blend, taken around the maximum of the Y6 T_1 feature between 1425 – 1475 nm. The clear fluence dependence of T_1 formation is indicative of a bimolecular generation pathway. **(c)** The trEPR spectra of the PM6:Y6 blend (80 K) after excitation at 532 nm, taken at 1 and 5 μs. The inset shows a magnification and simulation of the weak ISC triplet signal. The field positions of the absorption (*a*) and emission (*e*) EPR transitions of the ISC triplet are overlaid on the plot for clarity. **(d)** The IR region TA spectra of the PTB7-Th:IEICO-2F blend (293 K), excited with a moderate fluence of 3.8 μJ cm^{-2} at 620 nm for preferential PTB7-Th excitation. The IEICO-2F T_1 PIA at 1350 nm does not form in the blend. **(e)** The normalised TA kinetics of the PTB7-Th:IEICO-2F blend, taken around the maximum of the IEICO-2F T_1 PIA at 1350 – 1370 nm. No fluence dependence in the IEICO-2F T_1 region is observed. **(f)** The trEPR spectra of the PTB7-Th:IEICO-2F blend (80 K) after excitation at 532 nm, taken at 1 and 5 μs. The field positions of the absorption (*a*) and emission (*e*) EPR transitions of the ISC triplet are overlaid on the plot for clarity.

Figure 3: The role of hybridisation in organic solar cell blends. (a) The results of a rigid scan of the ^{1}CTE and ^{3}CTE energies for a representative PTB7-Th:IEICO-2F supramolecular configuration as a function of D:A separation. At each D:A separation, k_{BCT} from ^{3}CTE to T_1 of the NFA has also been calculated. The solid lines provide polynomial guides to the eye. **(b)** The results of a rigid scan of the ^{1}CTE and ^{3}CTE energies for a representative PM6:Y6 supramolecular configuration. At each D:A separation, k_{BCT} from ^{3}CTE to T_1 of the NFA has also been calculated. The solid lines provide polynomial guides to the eye. **(c)** A schematic to represent the effect of CTE-LE hybridisation on the energetic ordering of the ^{1}CTE and ^{3}CTE. **(d)** An image showing the same optimised supramolecular configuration between PTB7-Th (beige) IEICO-2F (purple) used for the calculations in Fig. 3a. The lobes represent regions of constructive overlap between the highest-occupied molecular orbitals (HOMOs) of D and A.

The HOMO overlap that controls the size of the electronic coupling and thus mediates hybridisation between the NFA LE and the CTEs; for hybridisation between the LE states of the D polymer and the CTEs, the lowest occupied molecular orbital overlap is the relevant interaction.